Supplemental Materials

Secular variation in seawater redox state during the Marinoan Snowball Earth event and implications for eukaryotic evolution

Weibing Shen, Xiangkun Zhu, Bin Yan, Jin Li, Pengju Liu, Simon W. Poulton

The WORD file includes:

- **Text S1**: **Geological Setting and Study Section Description**
- **Text S2**: **Glaciation System**
- **Text S3**: **Materials and Methods**
- **Text S4**: **Background and Interpretation of Geochemical Data**
- **Text S5**: **Alternative Hypotheses for Seawater Redox Variability**
- **Figure S1**: Global reconstruction of the location of the Yangtze block and stratigraphic division of the Neoproterozoic transect in the Yangtze block.
- **Figure S2**: Morphology of pyrite for Nantuo Formation in South China.
- **Figure S3**: Photographs showing lithofacies of the Nantuo Formation from the ZK01 core section.
- **Figure S4**: Model showing pyrite formation in the water column and sediments under oxic, ferruginous, and euxinic conditions.
- **References Cited**

Text S1: Geological Setting and Study Section Description

Geological Setting

South China consists of two tectonic units: The Cathaysia block in the present southeast, and the Yangtze block in the present northwest (Fig. 1a). The Yangtze block was an independent continental block during the late Neoproterozic, with direct connection to the open ocean to the southwest (Wang and Li, 2003; Fig. S1a).

Our samples from the Nantuo Formation were collected from a drill core (ZK01) from Taojiang city in northwestern Hunan Province, Yangtze block of South China (Fig. 1a). Neoproterozoic strata (Tonian strata, Cryogenian strata and Ediacaran strata) are well preserved on the Yangtze block, with some of the best age constraints in the world (Jiang et al., 2011; Fig. S1b). The Cryogenian strata include two glacial units separated by an interglacial interval (Zhang et al., 2011). The Chang'an Formation/Fulu Formation/Gucheng Formation/Tiesi'ao Formation, correspond to the Sturtian glaciation (ca.720-659 Ma; Wang and Li, 2003; Lan et al., 2015; Wang et al., 2019), and are mainly composed of diamictites. The interglacial strata, represented by the Datangpo Formation/Xiangmeng Formation, deposited from ca. 659 Ma to ca. 649 Ma (Zhou et al., 2018; Bao et al., 2018; Wang et al., 2019), and mainly comprise shale and siltstone with local manganiferous deposits (Zhang et al., 2015; Peng et al., 2019). The Nantuo Formation corresponds to the Marinoan glaciation, and mainly comprises glacial diamictite deposited between ca. 649 Ma to ca. 635 Ma (Condon et al., 2005; Zhang et al., 2008; Zhang et al., 2011; Schmitz 2012; Zhou et al., 2018; Bao et al., 2018; Wang et al., 2019). The Nantuo Formation, the target strata, has a wide distribution across the Yangtze block (Fig. 1b). The thickness of this unit varies significantly, from 60-100 m in shallow water settings such as the Hubei Yangtze Gorges area, through 200-300 m in slope settings such as the Guizhou Daotuo area,

to a few thousand meters in basin settings such as the Hunan Tongdao area (Fig. S1b; Wang and Li, 2003; Zhang et al., 2011).

As a whole, the Cryogenian Nantuo Formation has a conformable contact with the cap carbonate rocks of the overlying Ediacaran Doushantuo Formation across a basin-wide transect (Fig. S1b; Jiang et al., 2011; Lang et al., 2018a). Although the lithofacies of the two formations are obviously different, a conformable contact is observed (Lang et al., 2018a; Yan et al., 2020; Shen et al., 2021). On the one hand, as shown by a gradual upward increase in the calcareous content of the rocks in the top part of the Nantuo Formation, the lower glacial deposits progressively transform into a cap carbonate (Lang et al., 2018a; Yan et al., 2020; Shen et al., 2021). On the other hand, clastic gravels often appear at the bottom of the cap carbonate, representing a continuous transition between glacial and post-glacial deposits (Lang et al., 2018a; Yan et al., 2020; Shen et al., 2021).

The contact relationship between the Nantuo Formation and underlying non-glacial strata in the research area is complicated (Figs. 1b and S1b; Zhang et al., 2008; Peng et al., 2019; Yan et al., 2020; Shen et al., 2021). In shallow water settings, the Nantuo Formation has an unconformable contact with purple-red sandstone of the Liantuo Formation (Zhang et al., 2008; Peng et al., 2019; Yan et al., 2020; Shen et al., 2021). An unconformity between the Nantuo Formation and the Liantuo Formation is shown by deformation structures (Zhang et al., 2008; Peng et al., 2019; Shen et al., 2021). In slope-basin settings, the Nantuo Formation has a conformable contact with black shale of the Datangpo Formation/Xiangmeng Formation (Zhang et al., 2008; Peng et al., 2019; Yan et al., 2020; Shen et al., 2021). Although there are large changes in gravel content and size between the Nantuo Formation diamictite and the underlying interglacial shale of the Datangpo Formation/Xiangmeng Formation, no unconformity is observed. Instead, a gradual transition between

63 the two formations is evident in terms of colour, organic content and general lithology (Zhang et al.,
64 2008; Peng et al., 2019; Yan et al., 2020; Shen et al., 2021).

65 **Study Section Description**

66 The ZK01 core documents a slope-basin setting (Fig. 1a), and the Nantuo Formation from the
67 core has a conformable contact with the underlying interglacial Datangpo Formation mudstone and
68 the overlying Ediacaran Doushantuo Formation carbonate (Figs. S1b and 2). Thus, the Nantuo
69 Formation recovered from the core section was deposited during the Marinoan glaciation (Fig. 2).

70 The Nantuo Formation in ZK01 is about 295 m thick, and mainly comprises diamictite
71 lithofacies, with local fine-grained lithofacies (Fig. 2). The diamictite lithofacies in the Nantuo
72 Formation contains abundant pyrite (Fig. 2 and S2), and is mainly composed of dark gray gravel-
73 bearing carbonaceous sandstone, light gray gravelly siltstone, and dark gray-light gray siltstone (Figs.
74 2 and S3). This lithofacies is entirely matrix-supported and the gravels are poorly sorted, disordered,
75 and angular-shaped (subangular-circular and subangular dominate) (Figs. 2 and S3). The composition
76 of the gravels is diverse, although it is dominated by sandstone gravels and basic rock gravels. The
77 gravel content of the diamictite is generally greater than 5%, and locally greater than 30%. The gravel
78 sizes range from 2 mm to nearly 5 cm, with mm-scale size dominating. We emphasize here that the
79 gravel size and content show regular changes throughout the Nantuo Formation, marking two
80 lithological cycles (Fig. 2).

81 At the base, the Nantuo Formation from the core section conformably overlies the black shale
82 of the interglacial Datangpo Formation (Figs. 2 and S3). The first lithological cycle (0-125 m), begins
83 with a gravel sandy-mudstone interval, and mainly consists of dark-gray gravel-bearing carbonaceous
84 siltstone in the lower part, dark-grey gravelly sandstone in the middle part, and grey sandstone and

gravel-bearing siltstone in the upper part (Fig. 2). The gravel contents vary from < 10% at the bottom, through 30% in the middle, to < 10% at the top. Correspondingly, gravel sizes change from 0.2-1.5 cm, to 2.0-3.0 cm, and then back to 0.5-1 cm. The first cycle, as an entire shallowing-deepening sequence, ends with a ca. 4 m thickness of carbonate rock interval (Figs. 2 and S3). The second cycle (*ca* 125-295 m) mainly consists of light-grey gravel-bearing siltstone in the lower part, grey gravelly sandstone in the middle part, and light-grey calcareous gravel-bearing siltstone in the upper part. Similar to the first cycle, both the gravel content and size in this cycle first increase and then decrease. The gravel contents range from 0% to 25%, occasionally reaching 35%. Gravel sizes concentrate around 0.2-3 cm (generally 0.5-1 cm) (Fig. 2). The regular changes in gravel content and size indicate another entire shallowing-deepening sequence. At the top of the Nantuo Formation, post-glacial cap carbonate rocks of the Ediacaran Doushantuo Formation conformably overlie the diamictite (Figs. 2 and S3).

Text S2: Glaciation System

Glacial Sedimentology

Sedimentological characteristics of the Cryogenian successions are essential for interpreting the paleoenvironment in which these deposits formed. Based on distance from the ice grounding line, glacial facies can mainly be classified into ice-contact facies association, proximal glacial-marine facies association, and distal glacial-marine facies association (Boulton and Deynoux, 1981; Naish et al., 2009; Lang et al., 2018a). As is common in glacial sediments, proximal glacial-marine facies and distal glacial-marine facies are observed in the Cryogenian successions of South China.

The proximal glacial-marine facies association is mainly reflected by an assemblage of deposits formed near the ice grounding line (Brodzikowski and Van Loon, 1987). The sediments mainly

consist of meter-scale massive diamictite lithofacies and gravel-containing sandstones, which are usually deposited from gravity flow debris and rainout of ice-rafted debris transported by glaciers. The proximal glacial-marine facies association can be observed in the Nantuo Formation at multiple sections in South China, and mainly consists of thick massive diamictites (Fig. 1b; Shen et al., 2021). For example, evident massive diamictite lithofacies are developed in the lower part of the Nantuo Formation in the ZK01 core section, with thicknesses of more than 10 m (Fig. 2). When the flow pattern of subglacial meltwater drainage changes in the proximal glacialmarine environment, the resultant lithofacies will transform. This is shown by the transformation of thick massive diamictite lithofacies into other lithofacies, such as weakly sorted massive diamictite, gravel-bearing sandstones, and siltstones. There are many lithofacies transformations in the Nantuo Formation of South China. For example, in the upper part of the Nantuo Formation in the ZK01 core section, there are multiple massive diamictite-gravel sandstone cycles, which can be classified as a proximal glacial-marine facies association.

The distal glacial-marine facies association represents a set of sedimentary rocks formed in the environment far from the ice grounding line (Brodzikowski and Van Loon, 1987). This facies association can be observed in the Nantuo Formation at multiple sections in South China and mainly includes meter-scale massive diamictite lithofacies, gravel-containing fine-grained sandstones, and drop-stone lithofacies. For example, drop-stone lithofacies were observed in the Nantuo Formation at the Shennongjia section, South China (Fig. 1d). Because the distal glacial-marine environment is far from the ice grounding line, low density flow debris and gravity flow debris were deposited, with local transient medium or high density flow debris. Once the debris was carried to the area near the grounding line, it was deposited due to jet flows. Subsequently, the jet-flow deposits can be reworked

by flows in the shallow-water environment, winnowing the fine fraction and leaving gravel-bearing sandstones. Types of flow debris can be reflected by heterogeneous lithofacies: The coarse-grained sandstones with gravel always show high density flow debris, while the overlying sandstones and silts represent low density flow debris in a deeper water environment. The gravel-bearing coarse-grained sandstones in the Nantuo Formation in the ZK01 core section were likely deposited from high-density debris flows, which formed in a distal glacialmarine environment (Figs. 2 and S3). In addition, shales, siltstones and carbonates may be directly deposited from seawater with little glacial influence (Tucker et al., 1990; Łabaj and Pratt, 2016; Lang et al., 2018a), possibly in the distal glaciomarine environment or localised open water environment, as proposed by other studies (Lang et al., 2018a; Bai et al., 2020; Shen et al., 2021).

Based on sedimentary characteristics of the Nantuo Formation across a basin-wide transect, there is not only massive diamictite in the proximal glacial environment, but also gravel-containing fine-grained sediments in the distal glacial environment or the normal sea environment in South China (Fig. 4, Shen et al., 2021). The variations in the sedimentary facies of the Nantuo Formation in South China indicate that sedimentation was active during the glaciation.

Glaciation Dynamics

The initial ‘Snowball Earth’ hypothesis posited a simple, stagnant glaciation, characterized by extremely cold climate, and hence an entirely frozen Earth during the Cryogenian period (Kirschvink 1992; Hoffman et al., 1998). Although the ‘Snowball Earth’ hypothesis has become widely accepted (Hoffman and Schrag 2002; Boyle et al., 2007; Rooney et al., 2015), the interpretation of the simple, stagnant nature of the prolonged glaciations remains controversial. Debate has mainly focused on the interpretation of sedimentological records of glaciogenic strata throughout the Cryogenian ice age,

with data that indicate that the glaciations were dynamic rather than stagnant, and were associated with a relative strong climate and hydrological cycle.

The dynamic nature of the Cryogenian glaciation originally came from climate modeling. Hyde (2000) proposed rapid transitions into and out of a full glaciation, associated with decreased and increased temperatures, and an equatorial belt of open water that may have occurred during the 'Snowball Earth' event. The temperature fluctuations and changes in ice sheet extent were also deducted from follow-up simulations (Liu et al., 2020). These modeling results find support in sedimentary evidence. The key sedimentary records were vertical lithofacies alternations (Le Heron et al., 2014; Lang et al., 2018a; Hu et al., 2020; Yan et al., 2020). For example, studies from the Marinoan deposits in South China provide the basis for establishing a sequence stratigraphic framework that includes two complete glacial cycles across a basin-to-platform transect (Fig. 1b; Shen et al., 2021). Both cycles are characterized by repetition of glacially influenced units separated by non-glacial units. In addition, cyclic depositions of Marinoan units have been reported from elsewhere, such as Central Siberia (Chumakov, 2009), Oman (Allen and Etienne, 2008), Norway (Halverson et al., 2004), Southwest China (He et al., 2007), South Australia (Williams et al., 2008), and Scotland (Arnaud and Eyles, 2006). It is proposed that facies changes of the glacial deposits could be induced by excessive topography relief during the global glaciation (Hoffman et al., 2017b). In this scenario, deposition of diamictite during ice sheet melting may both create and destroy small-scale topography, resulting in short-distance migration of the depocenter and complexity in the stratigraphic detail of the glacial deposits. In particular, oversteepening of diamictite could generate reworked sediments, such as crudely stratified diamictite, pebbly sandstone and stratified sandstone (Hoffman et al., 2017b). This scenario seems to be a good explanation for variable thickness and

173 vertical facies change of glacial deposits within a short distance. However, it cannot explain the
174 stratigraphic variation of facies in the Nantuo Formation, which can be correlated across the Yangtze
175 block and has a basin-wide scale (Lang et al., 2018a; Shen et al., 2021). Further, the thick non-glacial
176 sequences (tens of meters) of siltstone/mudstones and carbonate beds in the Nantuo Formation cannot
177 simply be interpreted as deposits during ice sheet melting (Fig. 1b; Allen and Etienne, 2008; Lang et
178 al., 2018a; Gu et al., 2019). Instead, the massive diamictite and pebbly sandstone were precipitated
179 during the melting of ice sheet (Allen et al., 2004), while the clasts-free finegrained
180 mudstone/siltstone and sandstone represented normal marine deposition with siliciclastic sediments
181 transported by water currents (Talling et al., 2012). Thus, the repetition of glacially influenced units
182 separated by non-glacial units in the Nantuo Formation records ice-sheet advancing-retreating cycles
183 (Lang et al., 2018a; Bai et al., 2020; Shen et al., 2021).

184 Sedimentary records are a comprehensive reflection of paleoclimate changes and sea level
185 fluctuations (Hoffman and Schrag 2002). When the paleoclimate was cold, ice sheets would form,
186 sea level would drop, and hence the ice grounding line would advance seaward. Consequently, ice
187 advance successions dominated by a proximal glacial lithofacies association would be deposited, and
188 the gravel content and size of the rocks are increased (Lang et al., 2018a; Shen et al, 2021). By contrast,
189 when the paleoclimate warmed, the ice grounding line would retreat and sea level would rise. As a
190 result, ice retreat successions dominated by distal glacial lithofacies association would develop, and
191 the gravel content and size of the rocks decreases (Lang et al., 2018a; Shen et al, 2021). Thus, the
192 above-mentioned sedimentological records, interpreted to reflect gradual alternation from ice
193 advance to ice retreat, indicates dynamic co-evolution of the sedimentary environment, paleoclimate,
194 and sea level during the Marinoan glaciation (Lang et al., 2018a; Yan et al., 2020; Bai et al., 2020;

195 Shen et al., 2021).

196 The Marinoan deposits of the slope-basin ZK01 setting in South China also have two complete
197 glacial cycles (Fig. 2). The lower ice-advance succession of the glacial cycles consists primarily of a
198 massive diamictite lithofacies association, and is dominated by proximal glaciomarine deposits. The
199 gravel abundance and size of the deposits gradually increase upwards, suggesting a shallowing
200 sequence. The upper ice-retreat succession of the glacial cycles is composed of both a massive
201 diamictite lithofacies association and a fine-grained lithofacies association, representing a mix of
202 distal glaciomarine, proximal glaciomarine, and non-glacial marine deposits. The gravel abundance
203 and size of these varied deposits gradually decreases upwards, and is interpreted to reflect a deepening
204 sequence. These glacial cycles imply that the climate switched twice from relatively warm to
205 extremely cold and back during the Marinoan glaciation, associated with sea level fluctuations (Figs.
206 1, 2, and 4).

207 **Meltwater Supply**

208 Glacial meltwater can be divided into three categories: meltwater on the ice sheet surface
209 (atmospheric temperature), meltwater at the basal ice sheet (surface heat flow and pressure), and
210 meltwater at the base of the ice shelf (seawater temperature). The meltwater can form significant
211 drainage on the surface, internal and base of the glacier (Irvine-Fynn et al., 2011). Some of the
212 meltwater drainage on the ice sheet surface can reach the basal ice sheet through connected crevasses
213 and holes inside the glacier (Skidmore and Sharp, 1999). During the 'Snowball Earth' event,
214 subglacial meltwater drainage likely mainly consisted of meltwater from the basal ice sheet and the
215 basal ice shelf, with relatively little from the ice sheet surface.

216 Meltwater supply is closely related to the glacier thermal regime (Paterson, 2016), which is

controlled by air temperature (climate), geothermal flux, and pressure/friction (ice thickness) (Irvine-Fynn et al., 2011). When the geothermal flux and pressure are large (the glacier thickness is large), the glacier thermal regime would be warm, and there is a large amount of meltwater at the bottom of the glacier. Usually, connected meltwater drainages would occur at the warm basal ice sheet, causing the glacier to move quickly, thus depositing a large unit of glacial diamictite (Piotrowski, 1997). Conversely, the glacier thermal regime is colder when the geothermal flux and pressure are small. A cold glacier has less meltwater at the glacier base, and is mostly moved by internal ice deformation (Tranter et al., 1997). Generally, a thick ice sheet near the ice grounding line, where there is the fastest melting rate of glaciers, generates the largest amount of meltwater to form connected meltwater drainage (Lewis and Perkin, 1986). Glacial sedimentology and the relative abundance of different glacial facies can be used to interpret the thermal regime of ancient glaciers (Hambrey et al., 2012). Our sedimentary evidence above (Figs. 1b and 4) and previous studies have shown that Cryogenian glaciation with abundant diamictite may be a warm regime, leading to effective meltwater drainage in the South China region (Hu et al., 2020; Shen et al., 2021).

It is worth emphasizing that the amount of glacial meltwater supply varies with ice sheet dynamics (Hoffman et al., 2017). During the ice retreat period, the thickness of the glacier decreases and the amount of meltwater supply increases (Fig. 4). Meltwater production rates during this period may be an order of magnitude higher than the mean global runoff rate (Shields, 2005). A large amount of meltwater during this period can result in channelized meltwater drainage, which efficiently flows to the glaciomarine environment, discharging at the grounding line as focused meltstream exits (Piotrowski, 1997). During the ice advance period, the thickness of the ice sheet increases, the amount of meltwater supply decreases, and subglacial meltwater drainages are more widely distributed (Fig.

4). The distributed system is far less efficient than the channelized system, leading to longer meltwater residence times (Tranter et al., 1997).

Meltwater Derived-oxygen/sulfate

During the 'Snowball Earth' event, the global glaciation would have effectively ceased surface water–air/land communication, resulting in the extreme suppression of chemical cycles, including atmospheric oxygen and the continental sulfate influx (Kirschvink, 1992; Hoffman et al., 1998). However, injection of meltwater and the resultant drainage/stream generated beneath ice sheets can deliver sufficient dissolved oxygen and sulfate into the subglacial ocean (Liang et al., 2006; Anderson, 2007; Lechte et al., 2019).

Air bubbles trapped within the snow (meteoric ice) would be compressed into glacial ice (Hoffman et al., 2017). Upon melting of the glacier, either by increased air temperatures, geothermal fluxes, pressure or friction, meltwater would contain O_2 dissolved from the trapped air bubbles (Hoffman et al., 2017), as seen in modern Alpine glacial meltwater (Brown et al., 1994). Although this O_2 influx is supposed to be substantially offset by consumption of O_2 via either microbial or abiotic processes, such as seafloor weathering (Le Hir et al., 2008a), the remaining O_2 influx may be substantial (Anderson, 2007). Particularly, during the ice sheet retreat period, ice sheets melt significantly and channelized meltwater drainage is formed, and meltwater can convey O_2 to the subglacial environment (Jenkins, 1999), thus changing chemical properties such as seawater oxygenation (Le Hir et al., 2008a; Lechte et al., 2019).

Through a combination of friction and plucking, glaciers constantly erode the bedrock to form a large quantity of sediment, which fill the subglacial depositional space (Anderson, 2007). Due to the rapid rate of denudation and fine-textured nature of the sediments, glacial erosion produces a very

high overall mineral surface area. The substantial mineral surface area from glacial erosion significantly accelerates subglacial chemical weathering, and delivers a large amount of dissolved ions into glacial seawater via meltwater (Armstrong, 1971). For many glaciers, such as the Cascade Glacier, the ion influx related to subglacial weathering has been measured. These studies show that the total ion influx during the glaciation is generally in excess of the normal global mean (Hallet et al. 1996). As a major type of ion delivered into the subglacial seawater, sulfate, mainly derived from the oxidation of sulfide, accounts for about 10-25% of the total ion influx (Sharp et al. 1995; Anderson et al. 2000; Anderson et al. 2003). For example, at Bench Glacier (Alaska) on metamorphic sedimentary rocks, sulfate from the oxidation of sulfides accounts for 23% of the total ion influx into the ocean (Anderson et al. 2000). Thus, meltwater derived sulfate likely provided a significant flux to the Cryogenian subglacial ocean (Anderson, 2007; Hoffman et al., 2017).

Because the amount of meltwater discharge exerts an important control on subglacial oxygen (Liang et al., 2006; Lechte et al., 2019) and dissolved ion influx (Collins & MacDonald, 2004), it is most instructive to consider oxygen and sulfate fluxes as a function of water discharge (Anderson, 2007). With the glaciation dynamics and the associated dynamic meltwater supply, the delivery of dissolved oxygen and sulfate from meltwater generated beneath ice sheets varies with the ice advance and retreat (Fig. 4).

Text S3: Materials and Methods

Sample Description and Preparation

Samples for analysis of pyrite morphology, Fe-speciation, TOC and pyrite Fe-S isotopes were collected throughout the Nantuo Formation in the ZK01 core section of the Yangtze block, South China. Fragments of core samples were divided into two sub-samples, one for thin-section and

handpicking of pyrite grains, and the other for geochemical analyses.

Thin-sections (polished, 0.5-mm-thick) were used to investigate pyrite morphology. Pyrite, which is evident as larger euhedral grains in hand specimen (Fig. S2), is abundantly distributed throughout the Nantuo Formation. Under the optical and scanning electron microscope (SEM), pyrite morphologies vary, and include euhedral, subhedral, aggregates, disseminated pyrite and pyrite framboids (Figs. 2 and S2). A sample can contain more than one pyrite type, but euhedral and subhedral pyrite represent the dominant morphologies. The euhedral and subhedral pyrite are dominated by square and triangular pyrite, indicating a likely diagenetic origin. By contrast, detrital pyrite, which would be expected to have rounded grain boundaries, was not observed in the Nantuo Formation.

Prior to geochemical analyses of Fe-speciation and TOC, the matrix was sampled (finer grained sediments) in the bulk-rock samples to avoid larger clasts. Then, the matrix was powdered to <74 μm and preserved in a desiccator after being dried at 80°C for 3 h.

Total Organic Carbon (TOC)

TOC was determined at the State Key Laboratory of Petroleum Resources and Prospecting, China. To remove carbonate minerals, an appropriate amount of 10% HCl was used to dissolve the powdered matrix sample (about 0.5 g). The residue was washed with ultrapure water and then dried in a desiccator for 10 h at 60°C, followed by combustion at 900°C to oxidize organic carbon in a pure oxygen atmosphere. The resultant carbon dioxide was subsequently measured to provide the TOC data, using a LECO CS-230 carbon analyzer, and the detailed analytical procedure can be found in Zhao (2019).

Iron Speciation

Total iron (Fe_T) can be divided into three fractions: highly reactive iron (Fe_{HR}, representing the Fe fraction that is potentially reactive towards sulfidation in the water column and during diagenesis; Poulton and Canfield, 2011), poorly reactive iron (Fe_{PR}), and unreactive iron (Fe_U). Fe_{HR} includes: (1) iron associated with carbonate minerals (Fe_{carb}; siderite, ankerite); (2) ferric (oxyhydr)oxide minerals (Fe_{ox}; ferrihydrite, lepidocrocite, goethite, hematite); (3) magnetite (Fe_{mag}); and (4) Fe sulfide (Fe_{py}; pyrite) (Poulton and Canfield, 2005; Poulton and Canfield, 2011). Iron speciation analyses were performed at the University of Leeds, UK. Total Fe was extracted using a standard multi-acid digestion (HNO_3–HCl–HF) (Alcott et al., 2020), and the sequential extraction of Fe_{carb}, Fe_{ox} and Fe_{mag} was performed according to Poulton and Canfield (2005). All Fe concentrations were determined by atomic absorption spectrometry (AAS). Fe_{py} was extracted and measured at China University of Geosciences, Wuhan, via the chromous chloride reduction method of Canfield et al. (1986), with concentrations determined gravimetrically following precipitation of H_2S as Ag_2S. Accuracy and precision of all Fe phases was ensured by replicate extractions of international Fe speciation standard (Alcott et al., 2020), with a relative standard deviation of < 5% for all Fe pools.

Pyrite Sulfur Isotopes

Prior to sulfur isotope analysis, optical and scanning electron microscopy (SEM) were used to choose the pyrite crystals, and euhedral grains (> 50 μm) were selected. Thin sections with eligible pyrite grains were set into a sample cell coupled to the test instrument. Determination of sulfur isotope compositions was carried out by spot analysis, using a LA-MC-ICP-MS at the State Key Laboratory for Mineral Deposits Research, China, comprising a New Wave™ ArF excimer laser ablation system (UP-193FX, 193 nm, Fremont, America) coupled with a Neptune plus MC-ICP-MS (Thermo Fisher

Scientific™, Bremen, Germany). The operational conditions of the laser system and the MC-ICP-MS are from Zhu et al. (2016, 2017). An in-house pyrite standard (WS-1 with a $\delta^{34}S_{V\text{-}CDT}$ value of 0.3 ± 0.1‰, Zhu et al., 2016, 2017) was measured before and after each sample to calibrate the mass bias for S isotopes. In situ S isotope measurements were performed at medium mass resolution mode (Zhu et al., 2016, 2017).

Pyrite Iron Isotopes

Based on systematic observation of pyrite morphology, handpicking of large euhedral pyrite grains was carried out and the pyrite grains were cleaned ultrasonically in purified Milli-Q H_2O. About 10 mg handpicked pyrite grains were weighed in a beaker and digested using an acid mixture of ultra-pure concentrated HCl and HNO_3 at 120ºC. After evaporation of the HCl and HNO_3, the precipitate was dissolved and evaporated in 0.5 mL concentrated HCl three times. Then the remaining precipitate was diluted in 1.0 mL 6 N HCl. The solution for Fe extraction was purified using AGMP-1 resin, with polyethylene material as the exchange column (Φ6.8 mm×43 mm). The specific steps of AGMP-1 resin to separate iron in solution are described in Tang (2006a and 2006b). Measurement of Fe isotopes was performed on a Nu–MC–ICP–MS at the MLR Key Laboratory of Deep-Earth Dynamics, Institute of Geology, Chinese Academy of Geological Sciences. Specific method details are provided in Zhu (2002), Zhao (2012), and Fan (2014). Fe isotope values are reported in the standard notation as $\delta^{56}Fe$ deviation from IRMM-014. In order to monitor the accuracy of the $\delta^{56}Fe$ measurement, both international standard (BHVO-2) and a Chinese standard (CAGSR) were measured together with our samples. The external reproducibility was better than ±0.10‰ (Zhao et al., 2012; Fan et al., 2014).

Text S4: Background and Interpretation of Geochemical Data

Fe-speciation

Fe-speciation is a commonly used proxy for reconstructing seawater redox state. Fe_{HR}/Fe_T ratios > 0.38 generally indicate water column anoxia (Raiswell and Canfield, 1998; Canfield et al., 2008; Poulton and Canfield, 2011), whereas ratios in ancient rocks deposited under oxic conditions are generally significantly lower (0.14 ± 0.08; Poulton and Raiswell, 2002). However, due to inherent variability in the source rocks deposited in a particular region, wherever possible, an oxic baseline should be derived for the precise rocks being analysed (Raiswell et al., 2008; Poulton, 2021). Values between the oxic baseline and 0.38 are considered equivocal, as rapid deposition (as would likely be the case for the Nantuo Formation diamictites) or post-depositional conversion of unsulfidized Fe_{HR} to poorly reactive Fe minerals may lessen depositional Fe_{HR}/Fe_T ratios (Raiswell and Canfield, 1998; Poulton and Raiswell, 2002). In the case of equivocal Fe_{HR}/Fe_T ratios, additional evidence (e.g., $\delta^{56}Fe_{py}$ values) may allow oxic and anoxic deposition to be distinguished. Where samples are considered to have been deposited under anoxic conditions, Fe_{py}/Fe_{HR} ratios can be used to provide further inside into seawater redox state, whereby Fe_{py}/Fe_{HR} ratios > 0.6-0.8 indicate euxinic conditions (Raiswell and Canfield, 1998; Poulton and Canfield, 2005; Poulton, 2021) and Fe_{py}/Fe_{HR} radios < 0.6 indicate ferruginous conditions (anoxic, Fe(II)-containing; Poulton et al., 2004; Poulton, 2021).

Pyrite Sulphur Isotopes

The S isotope composition ($\delta^{34}S$) of sedimentary pyrite is mainly controlled by the S isotope composition of seawater sulfate and isotopic fractionation between sulfate and sulfide, both of which are essential for understanding the global sulfur cycle and pyrite S isotope systematics. Generally,

369 SO_4^{2-} concentrations in sediments or water column have the greatest impact on sulfur isotope
370 fractionations observed in sedimentary pyrite. When sulfate is present in abundance, microbial sulfate
371 reduction (MSR) can lead to sulfur isotope fractionations of up to 40‰ (Fig. S4). When SO_4^{2-}
372 concentrations are lower, the isotopic fractionation between SO_4^{2-} and H_2S may decrease. For
373 example, when the SO_4^{2-} concentration is lower than 200 μM, MSR has been shown to limit the extent
374 of sulfur isotope fractionation (Habicht et al., 2002).

375 Seawater sulfate, a key factor controlling S isotope fractionation, is mainly derived from the
376 oxidative weathering of sulfide on land, and seawater redox state exerts an influence on the burial
377 flux of sulfur. Thus, the seawater sulfate reservoir (SSR) is closely related to the redox state of the
378 atmosphere and ocean. In addition, $\delta^{34}S_{py}$ can provide information about the SSR and isotopic
379 composition of the seawater sulfate. Therefore, $\delta^{34}S_{py}$ is an effective general indicator of the size of
380 the SSR (e.g., Canfield, 1998). Although ^{32}S is preferentially -utilized by MSR, sulfur isotope
381 fractionation between sulfate and pyrite can become muted in the presence of limited sulfate supply
382 - leading to the formation of pyrite enriched in ^{34}S. Thus, a high $\delta^{34}S_{py}$ value may be linked to a
383 decrease in the SSR, which may be related to the expansion of anoxic waters and increased pyrite
384 burial (Scott et al., 2014).

385 **Pyrite Iron Isotopes**

386 The Fe isotope composition of sedimentary pyrite is controlled by the Fe isotope composition
387 of seawater and subsequent Fe isotopic fractionations during mineral formation, both of which form
388 the basis for explaining the $\delta^{56}Fe_{py}$ variability observed in our samples. Seawater Fe is mainly sourced
389 from continental weathering, riverine input, and submarine hydrothermal activity (Anbar and Rouxel,
390 2007), whereby (1) $\delta^{56}Fe$ values of igneous rocks are relatively uniform, concentrating around 0.1‰

391 (Zhu et al., 2002; Beard et al., 2003); (2) $\delta^{56}Fe$ values of continental weathering are slightly lower
392 than that of igneous rocks (~ -0.1‰; Anbar and Rouxel, 2007); (3) $\delta^{56}Fe$ values of the modern
393 submarine hydrothermal fluid varies from -0.8‰ to 0‰. (Yamaguchi et al., 2005); (4) Suspended and
394 dissolved iron from rivers accounts for more than 50% of the Fe source to seawater, and $\delta^{56}Fe$ values
395 range from -1.0‰ to 0‰ (Beard et al., 2003; Ingri et al., 2006); (5) $\delta^{56}Fe$ values of dissolved Fe
396 released from marginal sea and continental shelf sediments are close to that of igneous rocks
397 (Severmann et al., 2006). In summary, the iron isotopic composition of different sources generally
398 shows a certain degree of light isotope enrichment, explaining low $\delta^{56}Fe$ values in seawater through
399 the geological history. Sedimentary carbonate rocks are generally believed to record the $\delta^{56}Fe$
400 composition of seawater (von Blanckenburg et al., 2008). Yan et al. (2011) and Fan et al. (2014; 2018)
401 reported that the $\delta^{56}Fe$ values of carbonate rocks in the Ediacaran Doushantuo Formation, South
402 China, vary from −0.50‰ to 0‰. These $\delta^{56}Fe$ values suggest that seawater in South China during the
403 late Neoproterozoic era was enriched in the lighter iron isotopes. In our work, a $\delta^{56}Fe$ seawater value
404 of −0.50 to 0‰ has been assumed as a basis for interpreting pyrite iron isotope systematics.

405 The dynamic evolution of $\delta^{56}Fe_{py}$ in individual geologic terranes is dominantly interpreted to
406 reflect extensive/partial oxidation of seawater and subsequent iron reduction in sediments (Zhang et
407 al., 2015; Sawaki et al., 2017). Under oxic conditions, nearly all ferrous iron is completely oxidized
408 to ferric (oxyhydr)oxide minerals, minimizing the iron isotopic fractionation (Fig. S4a). The ferric
409 (oxyhydr)oxide is subsequently reduced in anoxic sediments, and may be converted into diagenetic
410 pyrite. The pyrite formed during early diagenesis has $\delta^{56}Fe$ values similar to, or lower than, seawater
411 (−0.8 to 0‰; Severmann et al., 2008), depending on the extent of reduction of the precursor iron
412 (oxyhydr)oxide minerals. Under ferruginous conditions, partial oxidation of ferrous iron may

commonly occur (Planavsky et al., 2012), resulting to significant iron isotopic fractionation of ~1 to 3‰, and formation of ferric (oxyhydr)oxides with high $\delta^{56}Fe$ values (Fig. S4b). Pyrite formed through the subsequently reduction of ferric minerals during early diagenesis may display large variability in $\delta^{56}Fe$ values, ranging from positive to negative, dependent on the $\delta^{56}Fe$ of the precursor iron (oxyhydr)oxide minerals and the extent of their reduction (Rouxel et al., 2005; Planavsky et al., 2012). Under euxinic (anoxic and sulfidic) conditions, ferrous iron undergoes extensive removal into pyrite, likely invoking an intermediate phase of FeS_m (Fig. S4c). Butler et al. (2005) suggest a kinetic isotopic fractionation (KIE) of 0.85 ± 0.30‰ ($\delta^{56}Fe$ value) during FeSm precipitation. Heard et al. (2020) also proposed that pyrite precipitation involves KIE, resulting in Fe^{2+} in FeS_2 being enriched in the lighter isotopes relative to $Fe^{2+}_{(aq)}$. However, as the FeSm-$Fe^{2+}_{(aq)}$ system gradually tends towards equilibrium, the kinetic fractionation value ($\delta^{56}Fe$ value) between Fe^{2+}aq and FeS_m gradually decreases, to < 0.3‰, or with no obvious fractionation (Butler et al., 2005; Guilbaud et al., 2010, 2011a, b). Thus, in this pathway of pyrite formation without an Fe (oxyhydr)oxide precursor, no significant iron isotopic fractionation occurs, and pyrite formed under euxinic conditions tend to have negative to near-zero $\delta^{56}Fe$ values (Severmann et al., 2008).

Redox state is the most important factor to control the fractionation of iron isotopes in the surface Earth, and pyrite iron isotopes can effectively trace ancient seawater redox conditions. Prior to interpreting $\delta^{56}Fe_{py}$ values, a possible detrital influence should be evaluated. Our detailed petrographic investigation did not find any robust evidence for substantial detrital pyrite in the Nantuo Formation at the ZK01 core (see sample description in the Materials and Methods above). Furthermore, the broad co-variation we observe among pyrite Fe isotopes, pyrite S isotopes and Fe-speciation is difficult to be explain unless the pyrite is syngenetic/diagenetic (Fig. 3). In particular,

435 the S isotope were from in-situ analysis of euhedral pyrite, and document progressive changes in
436 isotopic composition that are linked to independent evaluation of water column redox conditions.
437 This suggest that the variable Fe isotopic signatures of the Marinoan pyrite are unlikely to be related
438 to detrital input, and instead reflect a primary signal from syngenetic/diagenetic pyrite.

439 Text S5: Alternative Hypotheses for Seawater Redox Variability

440 Sea-level Elevation

441 Sea-level elevation, by controlling fluctuations in the depth and position of the chemocline, can
442 lead to variability in the redox state of the local seawater column, whereby sea-level falling and rising
443 may bring the seafloor at the study site into and out of the more oxygenated surface layer of the ocean.
444 Based on the abovementioned glaciation dynamics, ice advance and retreat are associated with sea-
445 level falling and rising. At the study section, the lithofacies and sedimentary characteristics show two
446 distinct ice advance-retreat cycles. For the first cycle, sea-level first falls and then rises during
447 deposition of Units I and Unit II, respectively, bringing the study site into and out of the more
448 oxygenated surface layer. However, all the geochemical data, including Fe-S isotopes and Fe-
449 speciation, indicate the opposite scenario, with deoxygenation and oxygenation occurring in upper
450 part of Unit I and Unit II, respectively (Fig. 3). Similarly, the ice advance recorded in the Unit III
451 corresponds to seawater deoxygenation (Fig. 3). These observations suggest that the redox variability
452 observed during the Marinoan glaciation was not caused by sea-level fluctuations.

453 Oxygen Input via Open Water

454 Another possible control on the dynamic redox history concerns the periodic development of
455 open water, leading to enhanced productivity and O_2 production, as well as exchange of O_2 between
456 the atmosphere and ocean. There is increasing evidence for open water conditions during the

Cryogenian glaciations. Ye et al. (2015) suggested that local open water conditions allowed the survival of benthic macroscopic phototrophs during the Marinoan glaciation. Elemental characteristics, Fe-speciation, and N-isotope data from Marinoan deposits also indicated expansive regions of open water throughout one of the harshest glaciations in Earth history (Johnson et al., 2017). In addition, red beds, carbonates and shales deposited in open water or glacial lakes have been identified in the glacial deposits (Lang et al., 2018a; Bai et al., 2020; Yan et al., 2020; Shen et al., 2021).

On the one hand, open water would enhance the supply of light to fuel photosynthesis, and hence O_2 production via organic matter production and burial. It has been suggested that no obvious mass extinction event is observed at this time from fossil records, biomarker evidence and molecular clock data (Erwin, 2015; Ye et al., 2015), although the low-latitude glaciation has been proposed to present a formidable barrier to the survival of oceanic species (Hoffman et al., 1998). Notably, active primary productivity occurred in the glacial ocean due to the open water (Johnson et al., 2017; Ye et al., 2015). Thus, we can assume that there was a certain amount of biogenically-produced O_2 in the glacial ocean. However, TOC concentrations recorded in our Nantuo Formation samples are low and relatively stable across the Nantuo Formation, giving no indication, at least at the local scale, of productivity-induced changes in O_2 production (Fig. 3).

On the other hand, open water allows air sea-gas exchange and oxygen diffusion into the subglacial ocean (Johnson et al., 2017), which could potentially lead to variability in seawater redox conditions. From geochemical calculations and numerical modelling, gas diffusion efficiency has a positive correlation relation with the ice-free surface size of the glacial ocean, but a limited area of open water (10^3 km^2) can lead to 90% modern efficiency, allowing an efficient gas diffusion into the

ocean (Le Hir, 2008a). Thus, equilibration of the atmosphere and ocean due to local open water was likely quite rapid (Le Hir, 2008a), and the chemical properties of seawater would thus change relatively rapidly (Le Hir, 2008b). Furthermore, given that open water is unsustainable because sea ice would become globally extensive within a few thousand years (Hoffman et al., 2017), rapid shutdown of the atmospheric O_2 influx would occur and seawater deoxygenation directly following rapid oxidation would be observed. This could be a prevalent cause of the shorter-term redox variability observed in parts of the Nantuo succession, but appears an unlikely explanation for the longer-term trends that are more closely linked to the broader cycles of glacial advance and retreat (Fig. 3).

Meltwater-derived Oxygen

As mentioned above, meltwaters can be a prominent source of oxygen to the subglacial ocean during 'Snowball Earth' events (Lechte et al., 2019). The geochemical evidence we present necessitates an explanation comprising well-oxygenated ice-retreat intervals and anoxic ice-advance intervals across two cycles during the Marinoan glaciation. We suggest that the most parsimonious explanation for these data comprises variable input of oxygen and sulfate from subglacial meltwaters.

In the beginning of the first ice advance during the glaciation, the ice sheet formed, and hence atmosphere O_2 influx was suppressed. As the ice became thicker, the influx of meltwater and its resultant O_2 was limited. The transient oxic conditions during this period (lower part of Unit I) could be interpreted as the initial persistence of a well-oxygenated interglacial ocean (Li et al., 2012; Zhang et al., 2015; Peng et al., 2019). With the ongoing first ice-sheet advance, the meltwater and resultant O_2 influx gradually decreased, leading to rapid consumption of seawater sulfate and the oxygen inventory. As a result, deoxygenation occurred and the previous oxic conditions transited to

501 anoxic/ferruginous conditions, albeit with fluctuations in redox state through upper part of Unit I (Fig.
502 3).

503 When the first ice-sheet retreat occurred, anoxic/ferruginous conditions initially persisted
504 through Unit II (Fig. 3). This increase in oxygenation occurred as the ice experienced it maximum
505 retreat, which was accompanied by an increasingly warm climate, leading to an abundant influx of
506 meltwater and subglacial water-filled rivers/streams containing O_2 (Anderson, 2007; Hoffman et al.,
507 2017).

508 The increase in oxygenation during the ice-sheet retreat period continued during the onset of
509 the second ice sheet advance, but it is terminated by the ongoing of the ice sheet advance. The oxic
510 conditions, interpreted by the finality of the previous seawater oxygenation, evolved into
511 anoxic/ferruginous conditions as the oxygenation level gradually decreased (Fig. 3). With the ongoing
512 of the second ice sheet advance, the climate turned colder and the ice sheet achieved its maximum
513 extent, thus decreasing the oxygen influx from meltwaters. In parallel, oxygen and sulfate would have
514 been consumed from the water column by microbial and abiotic processes, leading to the development
515 of anoxic/ferruginous conditions (Unit III).

516 The second ice retreat then occurred, with a substantial influx of sulfate leading to the
517 development of euxinic conditions recorded in Unit IV (Fig. 3). During this interval, enhanced
518 meltwater could have delivered abundant O_2 into the ocean. Nevertheless, a significant increase in
519 continental weathering, as proposed by the Mg isotopes (Huang et al., 2016), could have consumed
520 oxygen through oxidative weathering, and also delivered nutrients, ultimately resulting in the
521 development of water column euxinia (Lang et al., 2018b).

Spatial Significance

Our $\delta^{56}Fe_{py}$ and $\delta^{34}S_{py}$ data, as well as the Fe-speciation, record secular variability in seawater redox state during the Marinoan glaciation (Fig. 3). The secular variability in seawater redox state, although may be explained by a combination of meltwater-derived O_2 enhanced, productivity and O_2 production, as well as exchange of O_2 between the atmosphere and ocean, is evident in concert with the waxing and waning of the ice sheet (Fig. 4). The above-mentioned glaciation dynamics show the waxing and waning of the ice sheet, as well as the dynamic meltwater-derived O_2 influx, are tightly related to the temperature fluctuations and sea level evolution. Thus, the seawater redox variations deduced from those apparent regional proxies are actually controlled by global events, and as such they are of widespread significance.

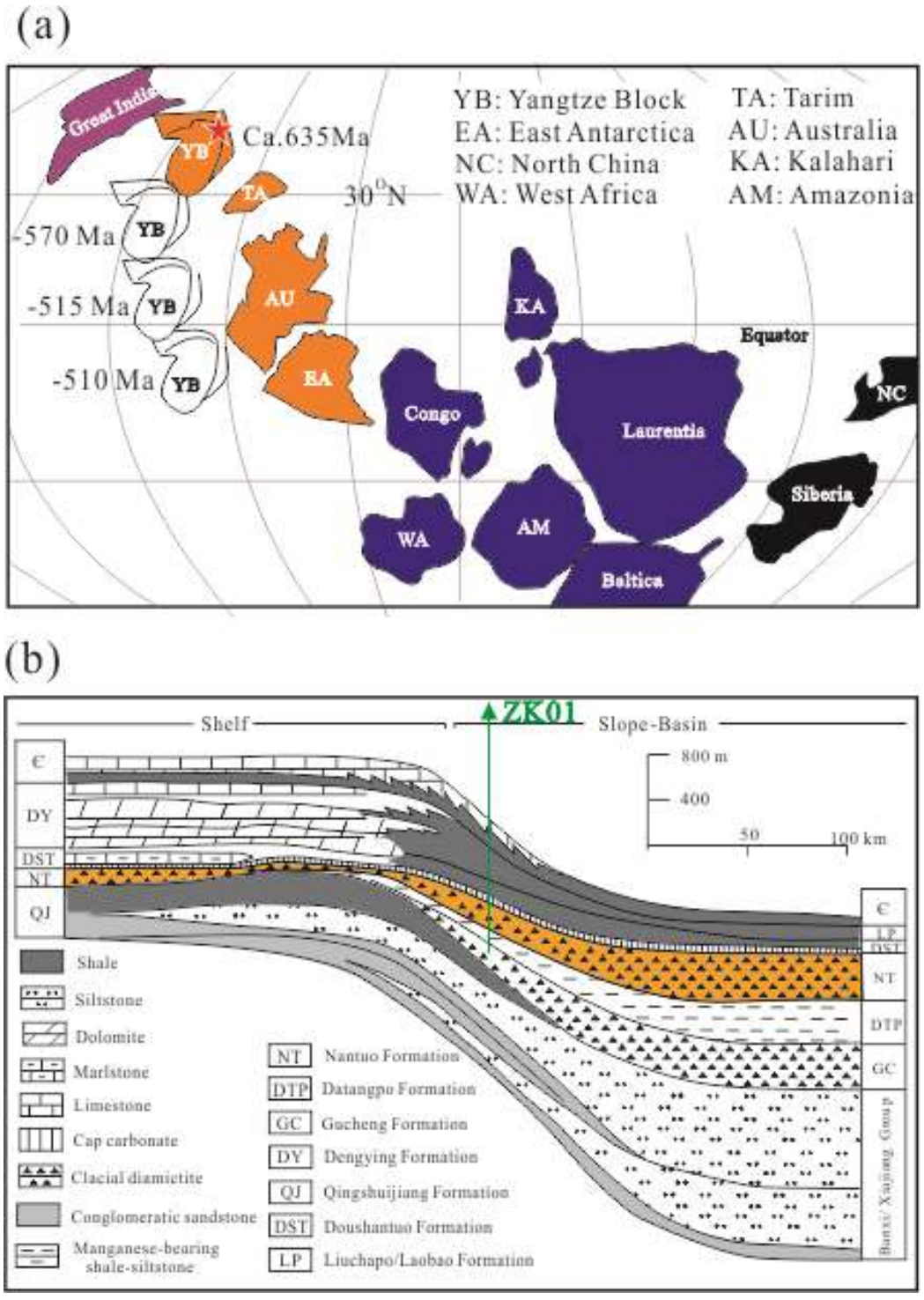

Figure S1

Global reconstruction of the location of the Yangtze block and stratigraphic division of the Neoproterozoic transect in the Yangtze block. (**a**) Global reconstruction of the location of the Yangtze block at ca. 635 Ma and drift trajectory from ca. 635 to ca. 510 Ma (simplified from Zhang et al., 2015). (**b**) Stratigraphic division of the Neoproterozoic transect from north to south in the Yangtze block (modified from Jiang et al., 2011). Location of drill core ZK01 can be seen in Fig. 1a.

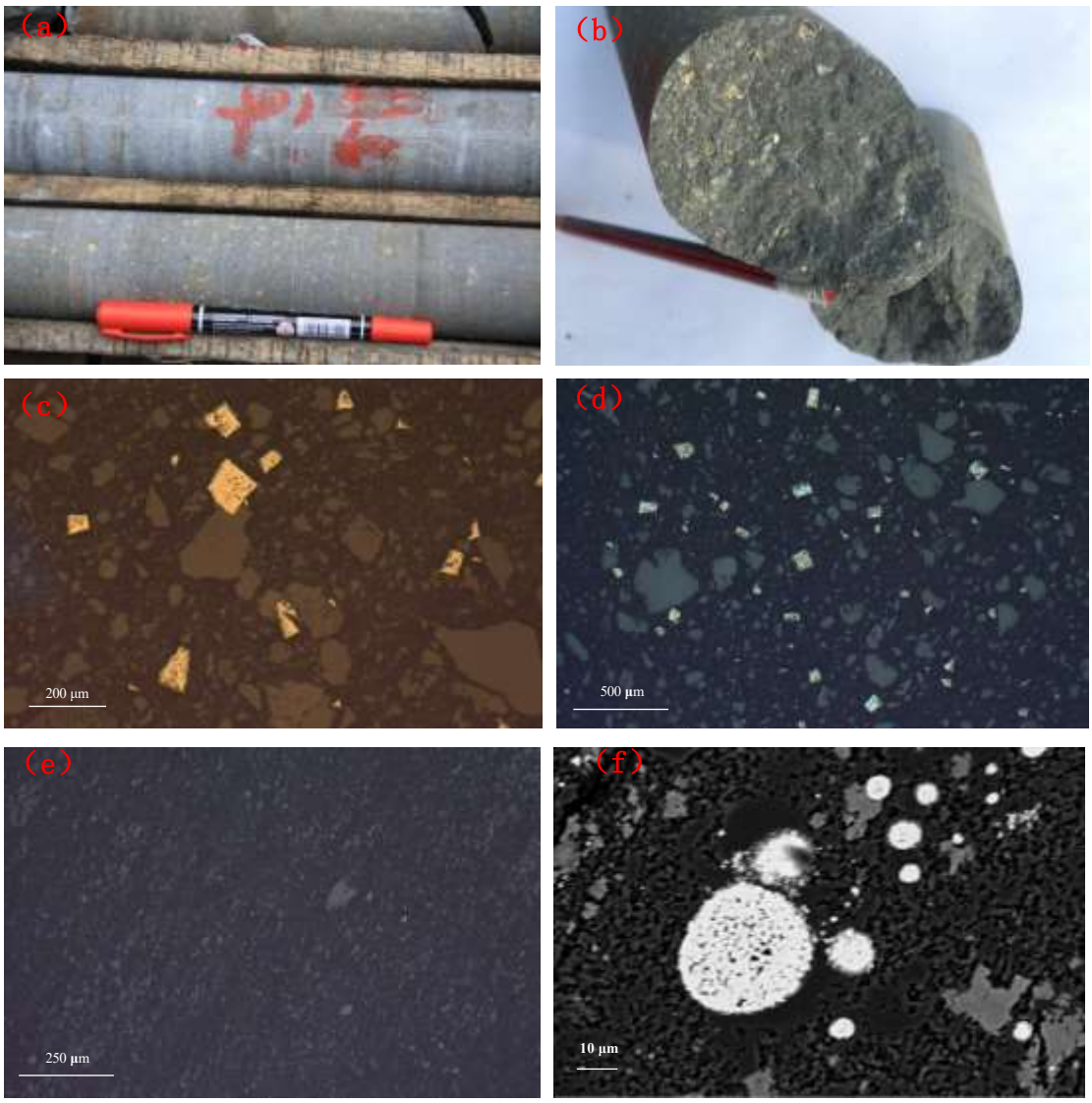

Figure S2

Morphology of pyrite for Nantuo Formation in South China. (**a**) and (**b**) show coarse-grained pyrite in hand specimen; (**c**) and (d) show euhedral pyrite under reflected light. (**e**) show disseminated pyrite under reflected light; (**f**) shows pyrite framboids under scanning electron microscope.

Figure S3

Photographs showing lithofacies of the Nantuo Formation from the ZK01 core section. (**a**) Nantuo Formation conformable overly the interglacial Datangpo Formation. (**b**) Manganese ore in the Datangpo Formation. (**c**) Diamictite lithofacies in the first lithological cycle. (**d**) Carbonate rock intervals between the two lithological cycles. (**e**) and (**f**), Diamictite lithofacies with small and large gravel size/content in the second lithological cycle. (**g**) Nantuo Formation conformably underlies the postglacial Doushantuo Formation. (**h**) Cap carbonate in the Doushantuo Formation.

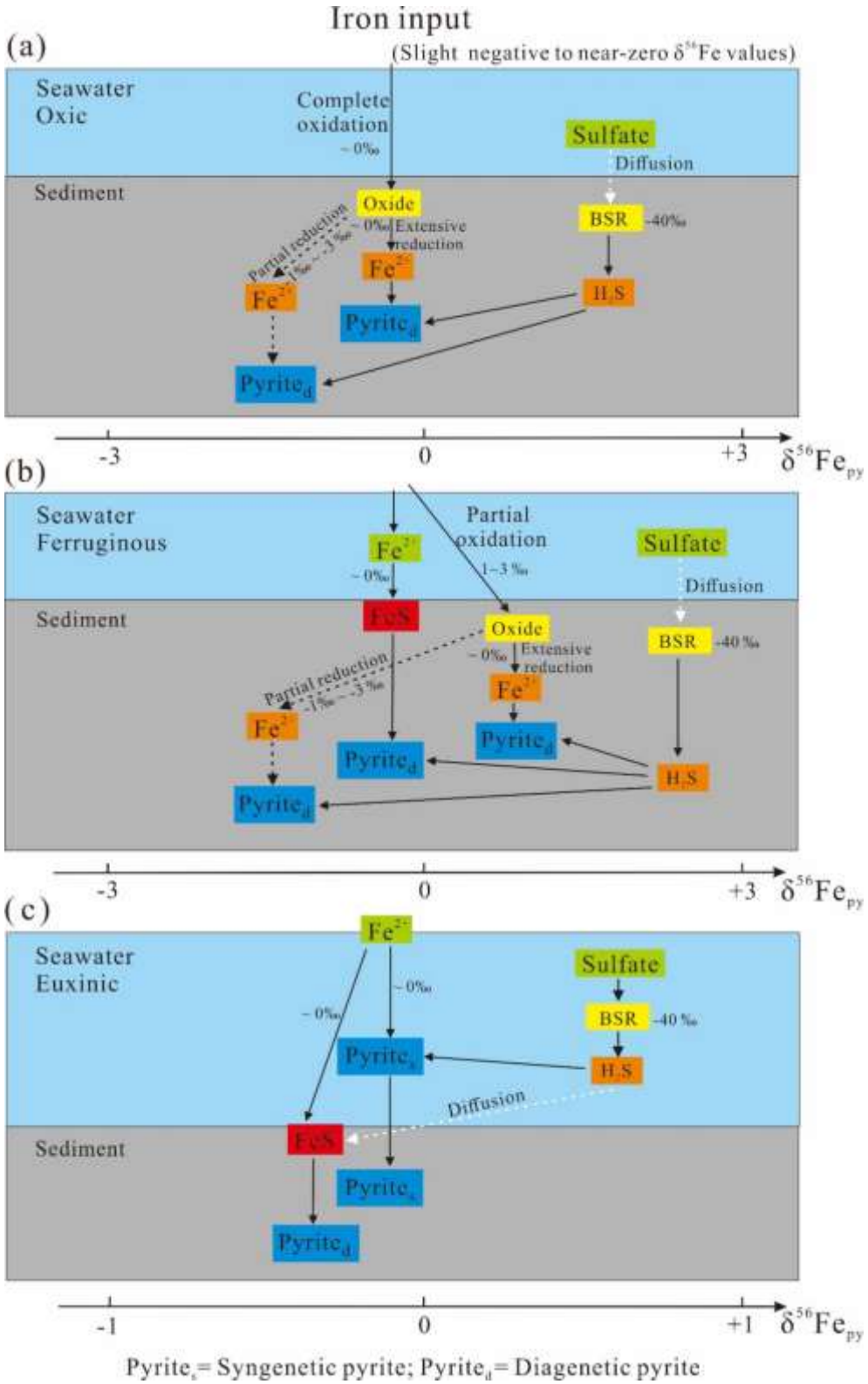

Figure S4

Model showing pyrite formation in the water column and sediments under (**a**) oxic, (**b**) ferruginous, and (**c**) euxinic conditions.

References Cited

Alcott, L. J., Krause, A. J., Hammarlund, E. U., 2020. Development of iron speciation reference materials for paleoredox analysis: Geostandards and Geoanalytical Research v. 44, p. 581–591.

Allen, P.A., Etienne, J.L., 2008, Sedimentary challenge to Snowball Earth: Nat. Geosci. v. 1, p. 817–825.

Allen, P.A., Leather, J., and Brasier, M.D., 2004, The Neoproterozoic Fiq glaciation and its aftermath, Huqf supergroup of Oman: Basin Res., v. 16, p. 507–534.

Anbar, A.D., Rouxel, O., 2007, Metal stable isotopes in paleoceanography: Annu. Rev. Earth Planet. Sci., v. 35, p. 717–746.

Anderson, S.P., 2007. Biogeochemistry of Glacial Landscape Systems: Annu. Rev. Earth Planet. Sci. v.35, p. 375–99.

Anderson, S.P., Drever, J.I., Frost, C.D., Holden, P., 2000, Chemical weathering in the foreland of a retreating glacier: Geochim. Cosmochim. Acta. v. 7, p. 1173–89

Anderson, S.P., Longacre, S.A., Kraal, E.R., 2003, Patterns of water chemistry and discharge in the glacier–fed Kennicott River, Alaska: evidence for subglacial water storage cycles: Chem. Geol., v. 3–4, p. 297–312

Armstrong, R.L., 1971, Glacial erosion and the variable isotopic composition of strontium in sea water: Nature, v. 230, p. 132–33

Arnaud, E., Eyles, C.H., 2006, Neoproterozoic environmental change recorded in the Port Askaig Formation, Scotland: Climatic vs tectonic controls: Sedimentary Geology, v. 183, p. 99–124.

Bai, H.Q., Liu, Y.Q., Peng, N. Kuang, H.W., and Wang, Y.C., 2020, Marinoan–aged red beds at Shennongjia, South China: Evidence against global–scale glaciation during the Cryogenian: Palaeogeography, Palaeoclimatology, Palaeoecology, v. 559 109967. doi:10.1016/j.palaeo.2020.109967.

Bao, X., Zhang, S., Jiang, G., Wu, H., Li, H., and Wang, X., 2018, Cyclostratigraphic constraints on the duration of the Datangpo Formation and the onset age of the Nantuo (Marinoan) glaciation in South China: Earth Planet. Sci. Lett., v. 483, p. 52–63.

Beard, B.L., Johnson, C.M., Von Damm, K.L., Poulson, R.L., 2003, Iron isotope constraints on Fe

cycling and mass balance in oxygenated Earth oceans: Geology, v. 7, p. 629.

Boulton, G. S., Deynoux, M., 1981, Sedimentation in glacial environments and the identification of tills and tillites in ancient sedimentary sequences: Precambrian Research, v. 15, p. 397–422.

Boyle, R.A., Lenton, T.M., Williams, H.T.P., 2007, Neoproterozoic 'snowball Earth' glaciations and the evolution of altruism: Geobiology, v. 5, p. 337–349

Brodzikowski, K., Van Loon, A., 1987, A systematic classification of glacial and periglacial environments, facies and deposits: Earth–Science Reviews, p. 297–381.

Brown, G., Tranter, M., Sharp M., Davies T., and Tsiouris S., 1994, Dissolved oxygen variations in Alpine glacial meltwaters: Earth Surface Processes and Landforms, v. 19, p. 247–253.

Butler, I.B., Archer, C., Vance, D., Oldroyd, A., Rickard, D., 2005, Fe isotope fractionation on FeS formation in ambient aqueous solution: Earth Planet. Sci. Lett., v. 236, p. 430–442.

Canfield, D.E., 1998, A new model for Proterozoic ocean chemistry: Nature, v. 396, p. 450–452

Canfield, D.E., Poulton, S.W., Knoll, A.H., et al., 2008, Ferruginous Conditions Dominated Later Neoproterozoic Deep–Water Chemistry: Science, v. 321, p. 949–952.

Canfield D.E., Raiswell R., Westrich J.T., Reaves C.M. and Berner R. A., 1986, The use of chromium reduction in the analysis of reduced inorganic sulfur in sediments and shales: Chem. Geol. V. 54, p. 149–155.

Condon, D.J., Zhu, M.Y., Bowring, S., Wang, W., Yang A.H., and Jin, Y.G., 2005, U-Pb ages from the Neoproterozoic Doushantuo Formation, China: Science v. 308, p. 95–98.

Collins, D.N., MacDonald, O.G., 2004, Year–to–year variability of solute flux in meltwaters draining from a highly–glacierized basin: Nordic Hydrol., v. 4–5, p. 359–67

Chumakov, N.M., 2009, Neoproterozoic glacial events in Eurasia. In: Gaucher, C., Sial, A.N., Halverson, G.P., Frimmel, H.E. (Eds.): Neoproterozoic–Cambrian Tectonics, Global Change and Evolution: a focus on southwestern Gondwana. Developments in Precambrian Geology 16, Elsevier, pp. 389–403.

Erwin, D. H., 2015, Early metazoan life: Divergence, environment and ecology: Philos. Trans. R. Soc. Lond. B Biol. Sci., v. 370, p. 36.

Fan, H.F., Wen, H.J., Zhu, X.K., Feng, L.J., and Chang, H.J., 2018, Oceanic redox condition during the late Ediacaran (551–541 Ma), South China: Geochimica et Cosmochimica Acta, v. 238,

59 p. 343–356.
60 Fan, H.F., Zhu, X.K., Wen, H.J., Yan, B., Li, J., and Feng, L.J., 2014, Oxygenation of Ediacaran
61 Ocean recorded by iron isotopes: Geochim. Cosmochim. Acta, v. 140, p. 80–94.
62 Gu S., Fu Y. and Long J., 2019, Predominantly Ferruginous Conditions in South China during the
63 Marinoan Glaciation: Insight from REE Geochemistry of the Syn-glacial Dolostone from the
64 Nantuo Formation in Guizhou Province, China: Minerals, v. 9.
65 Guilbaud, R., Butler, I.B., Ellam, R.M., Rickard, D., Oldroyd, A., 2011a. Experimental
66 determination of the equilibrium Fe isotope fractionation between Fe^{2+}_{aq} and FeS_m
67 (mackinawite) at 25 and 2℃: Geochim. Cosmochim. Acta, v. 75, p. 2721–2734.
68 Guilbaud, R., Butler, I.B., Ellam, R.M. 2011b. Abiotic pyrite formation produces a large Fe isotope
69 fractionation: Science, v. 332, p. 1548–1551.
70 Guilbaud, R., Butler, I.B., Ellam, R.M., Rickard, D., 2010, Fe isotope exchange between Fe(II)aq
71 and nanoparticulate mackinawite (FeSm) during nanoparticle growth: Earth Planet. Sci. Lett.,
72 v. 300, p. 174–183.
73 Habicht, K.S., Gade, M., Thamdrup, B., Berg, P., Canfield, D.E., 2002, Calibration of Sulfate Levels
74 in the Archean Ocean: Science, v. 298, p. 2372–2374.
75 Hambrey, M.J., Glasser, N. F., 2012, Discriminating glacier thermal and dynamic regimes in the
76 sedimentary record: Sedimentary Geology, p. 1–33.
77 Hallet, B., Hunter, L., Bogen, J., 1996, Rates of erosion and sediment evacuation by glaciers: a
78 review of field data and their implications: Global Planet. Change, v. 12, p. 213–35
79 Halverson, G.P., Maloof, A.C., Hoffman, P.F., 2004, The Marinoan glaciation (Neoproterozoic) in
80 Svalbard: Basin Res., v. 16, p. 297–324.
81 He, J.Y., Xu, B., Meng, X.Y., Kou, X.W., Liu, B., Wang, Y., Mi, H., 2007, Neoproterozoic sequence
82 stratigraphy and correlation in Quluqtagh area, Xinjiang: Acta Petrologica Sinica, v. 7, p.
83 1645–1654.
84 Heard, A.W., Dauphas, N., Guilbaud, R., Rouxel, O.J., Butler I.B., Nie, N.X., Bekker, A., 2020,
85 Triple iron isotope constraints on the role of ocean iron sinks in early atmospheric
86 oxygenation, Science, v. 370, p. 446–449.
87 Hoffman, P.F., Schrag, D.P., 2002, The snowball Earth hypothesis: testing the limits of global change:

Terra Nova, v. 14, p. 129–155.

Hoffman, P.F., Kaufman, A.J., Halverson, G.P., Schrag, D.P.A., 1998, Neoproterozoic Snowball Earth: Science, v. 281, p. 1342–1345.

Hoffman, P.F., Abbot, D.S., Ashkenazy, Y., Benn, D.I., Brocks, J.J., Cohen, P.A., Cox, G. M., Creveling, J.R., Donnadieu, Y., Erwin, D.H., Fairchild, I.J., Ferreira, D., Goodman, J.C., Halverson, G.P., Jansen, M.F., Le Hir, G., Love, G.D., Macdonald, F. A., Maloof, A.C., Partin, C.A., Ramstein, G., Rose, B.E.J., Rose, C.V., Sadler, P.M., Tziperman, E., Voigt, A., Warren, S.G., 2017a, Snowball Earth climate dynamics and Cryogenian geology–geobiology: Sci. Adv. v. 3, p. 1–43.

Hoffman, P.F., Lamothe, K.G., LoBianco, S.J.C., Hodgskiss, M.S.W., Bellefroid, E.J., Johnson, B.W., Hodgin, E.B., and Halverson, G.P., 2017b. Sedimentary depocenters on Snowball Earth: Case studies from the Sturtian Chuos Formation in northern Namibia: Geosphere, v. 13, p. 811–837.

Hu, C.L., Zhu, M.Y., 2020, Lithofacies and glacio–tectonicdeformation structures of the Tiesi'ao/Dongshanfeng Formation on the Yangtze Block, South China: Implications for Sturtian Glaciation dynamics: Palaeogeography, Palaeoclimatology, Palaeoecology, https://doi.org/10.1016/j.palaeo.2019.109481.

Huang, K.J., 2016, Episode of intense chemical weathering during the termination of the 635–Ma Marinoan glaciation. Proc. Natl Acad. Sci. v. 113, p. 14904–14909.

Hyde, W.T., Crowley, T.J., Baum, S.K., Peltier, W.R., 2000, Neoproterozoic'snowball Earth'simulations with a coupled climate/ice–sheet model: Nature, v. 405, p. 425–429.

Ingri, J., Malinovsky, D., Rodushkin, I., et al. 2006, Iron isotope fractionation in river colloidal matter: Earth and Planetary Science Letters, v. 245, p. 792–798.

Irvine‐Fynn, T. D., Hodson, A. J., Moorman, B. J., Vatne, G., Hubbard, A. L., 2011, Polythermal glacier hydrology: A review. Reviews of Geophysics, v. 4, p. RG4002.

Jenkins, A., 1999, The impact of melting ice on ocean waters: Journal of Physical Oceanography, v. 29, p. 2370–2381.

Jiang, G.Q., Shi, X.Y., Zhang, S.H., Wang, Y., and Xiao, S.H., 2011, Stratigraphy and paleogeography of the Ediacaran Doushantuo Formation (ca. 635–551 Ma) in South China: Gondwana Research, v. 19, p. 831–849.

Johnson, B.W., Poulton, S.W., and Goldblatt, C., 2017, Marine oxygen production and open water supported an active nitrogen cycle during the Marinoan Snowball Earth: Nature Communication, v. 8, p. 1316–1322.

Kirschvink, J.L., 1992, Late Proterozoic low–latitude global glaciation: the snowball Earth. In: The Proterozoic Biosphere: a multidisciplinary study: Cambridge University Press, New York, pp. 51–52.

Łabaj, M.A., and Pratt, B.R., 2016, Depositional dynamics in a mixed carbonate–siliciclastic system: middle–upper Cambrian Abrigo Formation, Southeastern Arizona, U.S.A: J. Sediment. Res., v. 86, p. 11–37.

Lan, Z., Li, X.H., Zhang, Q., and Li, Q.L., 2015, Global synchronous initiation of the 2nd episode of Sturtian glaciation: SIMS zircon U–Pb and O isotope evidence from the Jiangkou Group, South China: Precambr. Res., v. 267, p. 28–38.

Lang, X.G., Shen, B., Peng, Y.B., Xiao, S.H., Zhou, C.M., Bao, H.M., Kaufman, A.J., Huang, K.J., Crockford, P.W., Liu, Y.G., Tang, W.B., and Ma, H.R., 2018b, Transient marine euxinia at the end of the terminal Cryogenian glaciation: Nature communication, v. 9, p. 3019.

Lang, X.G., Chen, J.T., Cui, H., Man, L. Huang, K.J., Fu, Y., Zhou, C.M., and Shen, B., 2018a, Cyclic cold climate during the Nantuo Glaciation: Evidence from the Cryogenian Nantuo Formation in the Yangtze Block, South China: Precambr. Res., v. 310, p. 243–255.

Lechte, M.A., Wallace, M.W., Hood, A.S., Li, W.Q., and Planavsky, N.J., 2019, Subglacial meltwater supported aerobic marine habitats during Snowball Earth: Proc. Natl. Acad. Sci., v. 51, p. 25478–25483.

Le Heron, D.P., Busfield, M.E., Prave, A.R., 2014, Neoproterozoic ice sheets and olistoliths: multiple glacial cycles in the Kingston Peak Formation California: J. Geol. Soc., v. 171, p. 525–538.

Le Hir, G., Ramstein, G., Donnadieu, Y., and Goddéris, Y., 2008a, Scenario for the evolution of atmospheric pCO_2 during a snowball earth: Geology, v. 36, p. 47–50.

Le Hir, G., Godderis, Y., Donnadieu, Y., Ramstein, G., 2008b, A geochemical modelling study of the evolution of the chemical composition of seawater linked to a “snowball” glaciation: Biogeosciences, v. 5, p. 253–267.

Lewis, E., Perkin, R., 1986, Ice pumps and their rates. Journal of Geophysical Research: Oceans, p.

11756–11762.

Li, C., Love, G.D., Lyons, T.W., Scott, C.T., Feng, L.J., Huang, J., Chang, H.J., Zhang, Q.R., Chu, X.L., 2012, Evidence for a redox stratified Cryogenian marine basin, Datangpo Formation, South China: Earth and Planetary Science Letters, v. 331–332, p. 246–256

Liu, Y.G., Yang, J., Bao, H.M., Shen, B., Hu, Y.Y., 2020, Large equatorial seasonal cycle during Marinoan snowball Earth. Sci. Adv. 23, eaay2471. https://doi.org/10.1126/ sciadv.aay2471.

Naish, T., et al., 2009, Obliquity–paced Pliocene West Antarctic ice sheet oscillations: Nature, v. 458, p. 322.

Paterson S. B., The physics of glaciers (Elsevier, 2016).

Peng, X. Zhu, X.K., Shi, F.Q., Yan, B., Zhang, F.F., Zhao, N.N., Peng, P.A., Li, J., Wang, D., and Shields, G.A., 2019, A deep marine organic carbon reservoir in the non–glacial Cryogenian ocean (Nanhua Basin, South China) revealed by organic carbon isotopes: Precambrian Research, v. 320, p. 212–220.

Piotrowski, J. A., 1997, Subglacial hydrology in north–western Germany during the last glaciation: groundwater flow, tunnel valleys and hydrological cycles: Quaternary Science Reviews, v. 82, p. 169–185.

Planavsky, N., Rouxel, O.J., Bekker, A., Hofmann, A., Little, C.T.S., and Lyons, T.W., 2012, Iron isotope composition of some Archean and Proterozoic iron formations: Geochimica et Cosmochimica Acta, v. 80, p. 158–169.

Poulton, S.W., Fralick, P.W., Canfield, D.E., 2004, The transition to a sulphidic ocean~1.84 billion years ago: Nature, v. 431, p. 173–177.

Poulton, S.W., Canfield, D.E., 2011, Ferruginous Conditions: A Dominant Feature of the Ocean through Earth's History: Elements, v. 7, p. 107–112.

Poulton, S. W., and Canfield, D. E.., 2005, Development of a sequential extraction procedure for iron: implications for iron partitioning in continentally derived particulates: Chem. Geol., p. 209–221.

Poulton, S. W., and Raiswell, R., 2002, The low-temperature geochemical cycle of iron: From continental fluxes to marine sediment deposition. American Journal of Science, v. 302, p. 774–805

Poulton, S. W., 2021, The Iron Speciation Paleoredox Proxy: Elements in Geochemical Tracers in

178 Earth System Science: New York, Cambridge University Press, 1–19 p.
179 Raiswell, R., and Canfeld, D.E., 1998, Sources of iron for pyrite formation in marine sediments:
180 American journal of science, v. 298, p. 219–245.
181 Raiswell, R., Newton, R., Bottrell, S.H., Coburn, P.M., Briggs, D.E.G., Bond, D.P.G., Poulton, S.W.,
182 2008. Turbidite depositional influences on the diagenesis of Beecher's Trilobite Bed and the
183 Hunsruck Slate; sites of soft tissue pyritization. Am. J. Sci., v. 308, p. 105–129.
184 Rooney, A.D., Strauss, J.V., Brandon, A.D., Macdonald, F.A., 2015, A Cryogenian chronology: Two
185 long–lasting synchronous Neoproterozoic glaciations: Geology, v. 43, p. 459–462.
186 Rouxel, O.J., Bekker, A., and Edwards, K., 2005, Iron isotope constraints on the Archean and
187 Paleoproterozoic ocean redox state: Science, v. 307, p. 1088–1091.
188 Schmitz, M.D., 2012, Appendix 2—Radiometric ages used in GTS3012, in Gradstein, F., Ogg, J.,
189 Schmitz, M.D., and Ogg, G., eds., The Geologic Time Scale 2012: Boston, Elsevier, p.1045–
190 1082.
191 Scott, C., Wing, B.A., Bekker, A., Planavsky, N.J., Medvedev, P., Bates, S.M., Yun, M., and Lyons,
192 T.W., 2014, Pyrite multiple-sulfur isotope evidence for rapid expansion and contraction of the
193 early Paleoproterozoic seawater sulfate reservoir: Earth and Planetary Science Letters, v. 389,
194 p. 95–104.
195 Severmann, S., Johnson, C. M., Beard, B. L., McManus, J. 2006, The effect of early diagenesis on
196 the Fe isotope compositions of porewaters and authigenic minerals in continental margin
197 sediments: Geochim. Cosmochim. Acta, v. 70, p. 2006–2022.
198 Severmann, S., Lyons, T.W., Anbar, A., McManus, J., and Gordon, G., 2008, Modern iron isotope
199 perspective on the benthic iron shuttle and the redox evolution of ancient oceans: Geology, v.
200 36, p. 487–490.
201 Sharp, M., Tranter, M., Brown, G.H., Skidmore, M., 1995, Rates of chemical denudation and CO2
202 drawdown in a glacier–covered alpine catchment: Geology, v. 23, p. 61–64
203 Shen, W.B., Zhu, X.K., Yan, B., Qin, H.Y., Gao, Z.F., Li, F.B., 2021, Sequence stratigraphy of the
204 Cryogenian Nantuo Formation in South China: Constraints on Marinoan glaciation dynamics:
205 Journal of Asian Earth Sciences, v. 214, p. 104776.
206 Shields, G. A., 2005, Neoproterozoic cap carbonates: A critical appraisal of existing models and the

207 plumeworld hypothesis: Terra Nova, v. 17, p. 299–3102005.
208 Skidmore, M. L., Sharp, M. J., 1999, Drainage system behaviour of a High–Arctic polythermal
209 glacier: Annals of Glaciology, p. 209–215.
210 Sawaki, Y., Tahata, M., Komiya, T., Hirata, T., Han, J., and Shu, D.G., 2018. Redox history of the
211 Three Gorges region during the Ediacaran and Early Cambrian as indicated by the Fe isotope:
212 Geoscience Frontiers, v. 9, p. 155-172.
213 Talling P.J., Masson D.G., Sumner E.J. and Malgesini G., 2012, Subaqueous sediment density flows:
214 Depositional processes and deposit types: Sedimentology, v. 59, p. 1937–2003.
215 Tang, S.H., and Zhu, X.K., 2006a, Separation of some element using AG MP–1 anion exchange
216 resin: Geological journal of China university, v. 3, p. 398–403.
217 Tang, S.H., Zhu, X.K., Cai, J.J., Li. S.Z., He, X.X., and Wang, J.H., 2006b, Chromatographic
218 separation of Cu, Fe and Zn using AG MP–1 anion exchange resin for isotope determination
219 by MC–ICPMS: Rock and mineral analysis, v. 1, p. 5–8.
220 Tostevin, R., Turchyn, A.V., Farquhar, J., et al. 2014, Multiple sulfur isotope constraints on the
221 modern sulfur cycle, Earth and Planetary Science Letters, v. 396, p. 14–21
222 Tranter et al., 1997, Variability in the chemical composition of in situ subglacial meltwaters:
223 Hydrological Processes, p. 59–77.
224 Tucker, M.E., Paul Wright, V., and Dickson, J.A.D., 1990, Carbonate Sedimentology. Blackwell p.
225 28–67.
226 von Blanckenburg, F., Mamberti, M., Schoenberg, R., et al. 2008, The iron isotope composition of
227 microbial carbonate: Chemical Geology, v. 249, P. 113–128.
228 Wang, D., Zhu, X.K., Zhao, N.N., Yan, B., Li, X.H., Shi, F.Q., and Zhang, F.F., 2019, Timing of the
229 termination of Sturtian glaciation: SIMS U–Pb zircon dating from South China: J. Asian Earth
230 Sci., v. 177, p. 287–294.
231 Wang, J., and Li, Z.X., 2003, History of Neoproterozoic rift basins in South China: implications for
232 Rodinia break–up: Precambrian Research, v. 122, p. 141–158.
233 Williams, G.E., Gostin, V.A., McKirdy, D.M., Preiss, W.V., 2008, The Elatina glaciation, Late
234 Cryogenian (Marinoan Epoch), South Australia: Sedimentary facies and palaeoenvironments:
235 Precambr. Res. V. 163, P. 307–331.
236 Yamaguchi, K. E., Johnson, C. M., Beard, B. L., and Ohmoto, H., 2005, Biogeochemical cycling of

237 iron in the Archean–Paleoproterozoic Earth: constraints from iron isotope variations in
238 sedimentary rocks from the Kaapvaal and Pilbara Cratons: Chem. Geol., v. 218, p. 135-169.
239 Yan, B., 2011, Geochemical characteristics of carbonate rocks and black shale in Doushantuo
240 Formation of Ediacaran System, South China. Beijing: Doctoral dissertation of China
241 University of Geosciences (Beijing).
242 Yan, B., Shen, W.B., Zhao, N.N., and Zhu, X.K., 2020, Constraint on the nature of Marinoan
243 glaciation: Cyclic sedimentary records of the Nantuo Formation, South China: Journal of
244 Asian Earth Sciences, v.189, 104137 (1–13).
245 Ye, Q., Tong, J.N., Xiao, S.H., Zhu, S.X., An, Z.H., Tian, L., and Hu, J., 2015, The survival of
246 benthic macroscopic phototrophs on a Neoproterozoic snowball Earth: Geology, v. 43, p.
247 507–510.
248 Zhang, F.F., Zhu, X.K., Yan, B., Kendall, B., Peng, X., Li, J., Algeo, T.J., and Romaniello, S., 2015.
249 Oxygenation of a Cryogenian ocean (Yangtze Basin, South China) revealed by pyrite Fe
250 isotope compositions: Earth Planet. Sci. Lett., v. 429, p. 11–19.
251 Zhang, Q. R., Chu, X. L., and Feng, L.J., 2011, Chapter 32 Neoproterozoic glacial records in the
252 Yangtze Region, China. In: Arnaud, E., Halverson, G.P., Shields–Zhou, G. (Eds.), The
253 Geological Record of Neoproterozoic Glaciations. vol. 36. Geological Society, London,
254 Memoirs, v. 36, p. 357–366.
255 Zhang, S., Jiang, G., and Han, Y., 2008, The age of the Nantuo Formation and Nantuo glaciation in
256 South China: Terra Nova, v. 20, p. 289–294.
257 Zhao, J.H., Jin, Z.J., Hu, Q.H., Liu, K.Y., and Wang, R.Y., 2019, Geological controls on the
258 accumulation of shale gas: A case study of the early Cambrian shale in the Upper Yangtze
259 area: Marine and petroleum geology, v. 107, p. 423–437.
260 Zhao, X.M., Zhang, H.F., Zhu, X.K., Tang, S.H., and Yan, B., 2012, Iron isotope evidence for
261 multistage melt–peridotite interactions in the lithospheric mantle of eastern China: Chem.
262 Geol., v. 292–293, p. 127–139.
263 Zhou, C.M., Tucker, R., Xiao, S.H., Peng, Z.X., Yuan, X.L., and Chen, Z., 2018, New constraints
264 on the ages of Neoproterozoic glaciations in south China: Geology, v. 32, p. 437–440.
265 Zhu, X.K., Guo, Y., Williams, R.J.P., O'Nions, R.K., Matthews, A., Belshaw, N.S., Canters, G.W.,
266 Waal de, E.C., Weser, U., and Burgess, B.K., 2002, Mass fractionation processes of transition

metal isotopes: Earth Planet. Sci. Lett., v. 200, p. 47–62.

Zhu, Z.Y., Jiang, S.Y., Ciobanu, C.L., Yang, T., Cook, N.J., 2017, Sulfur isotope fractionation in pyrite during laser ablation: Implications for laser ablation multiple collector inductively coupled plasma mass spectrometry mapping: Chemical Geology, v. 450, p. 223–234

Zhu, Z.Y., Cook, N.J., Yang, T., Ciobanu, C.L., Zhao, K.D., and Jiang, S.Y., 2016, Mapping of sulfur isotopes and trace elements in sulfides by LA–(MC)–ICP–MS: Potential Analytical Problems, Improvements and Implications: Minerals, v. 110, p. 1–14.